

Non-equilibrium precondensation of classical waves in two dimensions propagating through atomic vapors

Neven Šantić^{1,2}, Adrien Fusaro³, Sabeur Salem¹, Josselin Garnier⁴, Antonio Picozzi³, Robin Kaiser¹

¹ Université Côte d'Azur, CNRS, Institut de Physique de Nice, Valbonne F-06560, France

² Institute of Physics, Bijenička cesta 46, 10000 Zagreb, Croatia

³ Laboratoire Interdisciplinaire Carnot de Bourgogne, CNRS,

Université Bourgogne Franche-Comté, Dijon, France and

⁴ Centre de Mathématiques Appliquées, Ecole Polytechnique, 91128 Palaiseau Cedex, France

Nonlinear Schrödinger model

The D2-line of rubidium at $\lambda \approx 780\text{nm}$ is composed of several hyperfine transitions, including 2 hyperfine ground states and 4 excited state hyperfine levels for each of the two natural isotopes present in our vapour cell. Close to the atomic resonance, Doppler broadening of $k_0 v \approx 270\text{MHz}$ at $T \approx 150^\circ\text{C}$ yields a Gaussian transmission profile for each of these lines which can be taken into account by proper convolution. At sufficient large detunings however, the Lorentzian shape due to the natural line of $\Gamma = 6.06\text{MHz}$ becomes dominant and we will thus neglect such Doppler broadening for detunings larger than $|\Delta| > 1\text{GHz}$. In this limit, we can model the response function of our vapor cell for the complex amplitude A of the electric field as based on an effective two-level atom [1]:

$$\partial_z A = \frac{i}{2k_0} \nabla^2 A - i\sigma_0 \frac{2\Delta/\Gamma - i}{1 + 4\Delta^2/\Gamma^2 + I/I_s} A \quad (\text{S1})$$

with $\sigma_0 = 3\pi\rho_{at}/k_0^2$, ρ_{at} being the density of atoms, k_0 the wave number of the laser beam, I_s the saturation intensity and $I = |A|^2$ describing the intensity of the electric field. Note that the nonlocal character of the nonlinearity in atomic vapours [20] has been neglected here and its influence on the effect of precondensation will be discussed later through the numerical simulations. The linear part of the atomic polarisability can be absorbed by defining

$$\psi(\mathbf{r}, z) = A(\mathbf{r}, z) \exp\left(i\sigma_0 \frac{2\Delta/\Gamma}{1 + 4\Delta^2/\Gamma^2} z\right) \quad (\text{S2})$$

leading to the nonlinear propagation equation

$$i\partial_z \psi = -\frac{1}{2k_0} \nabla^2 \psi + \frac{\gamma|\psi|^2}{1 + \alpha|\psi|^2} \psi - \frac{i\sigma_0}{1 + 4\Delta^2/\Gamma^2 + |\psi|^2/I_s} \psi \quad (\text{S3})$$

where the nonlinear coefficient is $\gamma = -2\sigma_0\Delta\mu^2/(\Gamma I_s)$, with $\mu = 1/(1 + 4\Delta^2/\Gamma^2)$. With these parameters we have a saturation of the nonlinearity described by $\alpha = \mu/I_s$. Note that we will assume negative detuning ($\Delta < 0$) so as to ensure a defocusing nonlinearity. It is important to note that the experiments have been carried out at large negative detuning, where we can neglect light absorption in the cell, i.e., the last term in Eq.(S3). For instance, the experimental results shown in Fig. 3 of the main text have been obtained by changing for each correlation length σ_c the healing length Λ via the laser detuning. The smallest value of Λ (i.e., largest nonlinearity) is obtained when the laser frequency approaches the atomic resonance frequency, where residual absorption starts to lower the total transmission through the cell. Except for the three points at largest L/Λ for each value of σ_c , the transmission coefficient is above 70%. In this

regime of large detuning, we will thus neglect the residual absorption (corresponding to the last term in Eq. (S3)) as well as the saturation of the nonlinearity (corresponding to the term in α in Eq. (S3)). Equation (S3) can thus be rewritten as the NLS Eq. (1) in the main text.

Calibration of nonlinearity

The nonlinear response of our rubidium vapour cell is characterized by the accumulated nonlinear phase shift during propagation. We calibrate this nonlinearity by detecting the far field of a Gaussian beam with a waist (intensity at $1/e^2$) of $\omega = 1.7\text{ mm}$ after propagation through the same Rb cell. For a defocusing nonlinearity diffraction rings appear in the far field. Counting the number of rings, n , allows us to determine the absolute accumulated nonlinear phase shift Φ_{NL} at the beam centre, as the nonlinear phase is related to the number of rings by $\Phi_{NL} = 2n\pi$ for a maximum intensity at the centre of the far field or $\Phi_{NL} = (2n - 1)\pi$ for a minimum at the centre [2–6]. Examples of the far field images are shown as insets in Fig. S1. We count the number of rings for different detunings of the laser at fixed total powers, Fig. S1, and for different powers at fixed detunings, Fig. S2.

Using the effective two level system to model our medium and for large detunings $\Delta \gg \Gamma$ (a condition met in our experiment), the nonlinear phase shift Φ_{NL} , proportional to the nonlinear refractive index $\Delta n = n_2 I$, is given by:

$$\Phi_{NL} = k_0 L n_2 I \propto \frac{I}{I_s} \frac{1}{\Delta} \frac{1}{4\Delta^2/\Gamma^2 + I/I_s}, \quad (\text{S4})$$

The lines in Fig.S1 and Fig.S2 correspond to fits using Eq.(S4), taking I_s and the zero frequency for the detuning as a free parameters to account for multiple rubidium lines contributing to the nonlinearity. Using the results of these fits, we can determine the nonlinear phase shift for an arbitrary choice of intensity and detuning.

In the experiment with an initial speckle field, the relevant nonlinear phase shift will be defined as an average over an area of interest (AOI). We therefore fit the speckle field with a Gaussian envelope and take the average intensity inside a ω_{1/e^2} diameter of the Gaussian beam. From the nonlinear phase shift extracted from such an average intensity, we compute the nonlinear length scale $z_{NL} = 1/k_0 \Delta n = L/\Phi_{NL}$ and the corresponding healing length $\Lambda = \sqrt{z_{NL}/(2k_0)} = \sqrt{L/(2k_0 \Phi_{NL})}$ used for Fig. 3(a-b).

We also monitor the atom density in all measurements by observing the absorption of a very weak probe beam from a separate DFB laser (total incident power $P_{probe} < 10\text{ }\mu\text{W}$) while scanning over all four Rb lines. A typical absorption spectrum is show in Fig. S3. We fit an adequate Doppler-broadened model to the transmission profile with which we determine the atom density. Typical atom densities used in

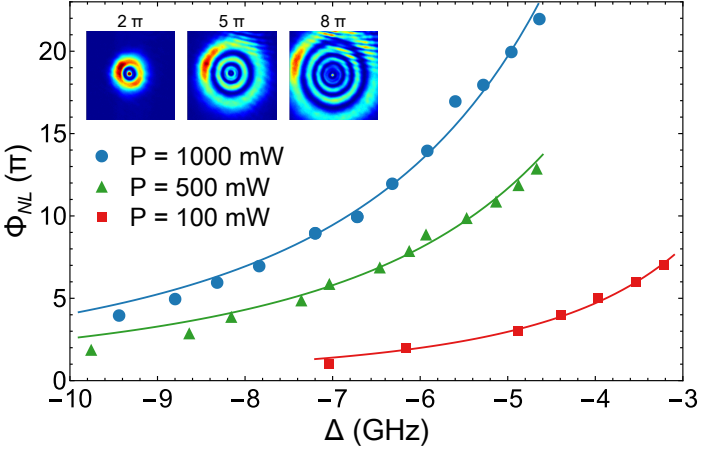


FIG. S1: Calibration of the nonlinearity as a function of laser frequency The calibration was performed for three different incident powers: 100mW (red squares), 500mW (green triangles) and 1000 mW (blue circles) respectively. The frequency, Δ is the laser detuning from the $|5S_{1/2}; F = 2\rangle \rightarrow |5P_{3/2}; F' = 3\rangle$ transition in ^{87}Rb . Solid lines are fitted functions (see text for details). Insets show examples of far field images. Note the lack of a central maximum for the 5π case.

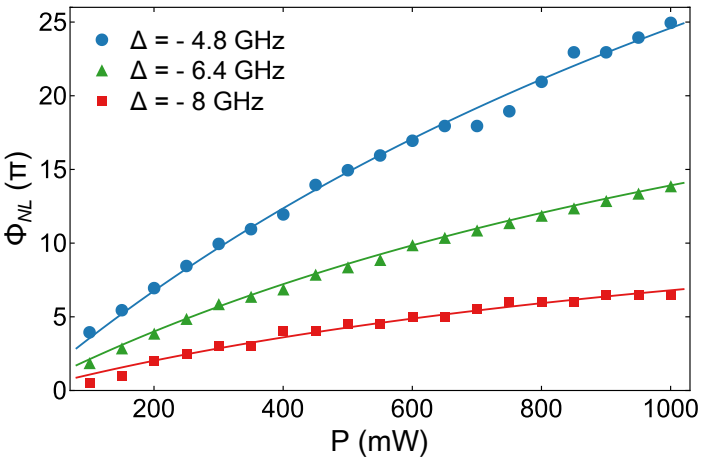


FIG. S2: Calibration of the nonlinearity as a function of incident power P The calibration was performed for three different laser detunings: $\Delta = -4.8 \text{ GHz}$ (blue circles), $\Delta = -6.4 \text{ GHz}$ (green triangles) and $\Delta = -8 \text{ GHz}$ (red squares), respectively. Solid lines are fitted functions (see text for details).

the experiment are $\rho_{at} \approx 2 \times 10^{20} \text{ m}^{-3}$.

Correlations length and Area of Interest

We characterize the speckle field, obtained by passing a 1W fiber laser (EYLSA-L-780.24-1.0-P-SS-W-FC, Quantel) beam through a narrow angle (0.5° , 10DKIT-C1, Newport) diffuser, by the correlation length of the intensity, which we extract from the 2D near field images. An example of a near field image is shown in Fig. S4 (a). The images are taken with a CCD camera (GRAS-20s4m) with a commercial 50 mm objective, depicted in Fig. 1 as an effective single lens, L2. A spacer between the objective and the camera increases the distance of L2 from the CCD chip, 50 mm in length, giving a total distance between L2 and the CCD of 100 mm,

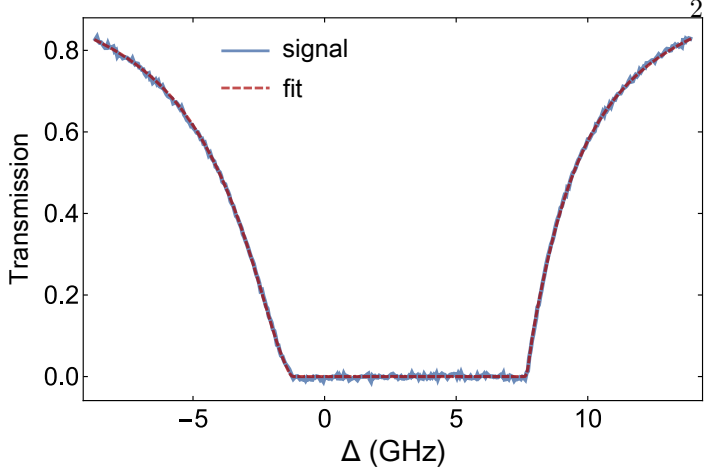


FIG. S3: Calibration of atom density. The atomic density is adjusted by heating the vapour cell to $\approx 150^\circ\text{C}$. We extract the value of the atomic density by fitting the low intensity transmission profile taking into account all Doppler broadening lines of rubidium at 780nm.

and thus a magnification of $M = 1$, confirmed by imaging a calibration target placed on the output face of the rubidium cell. With a magnification of unity the resolution of the near field images is given by the pixel size on the CCD chip of $4.4 \mu\text{m}$.

We extract the spatial correlation function of the speckle field from the intensity autocorrelation function of these near field images $I(\mathbf{r}')$. Using the Wiener-Khinchin theorem we compute this intensity correlation function by $C_I(\mathbf{r}) \propto \int e^{-i\mathbf{k} \cdot \mathbf{r}} |\int I(\mathbf{r}') e^{i\mathbf{k} \cdot \mathbf{r}'} d\mathbf{r}'|^2 d\mathbf{k}$. This 2D autocorrelation function has a pronounced peak in the center, see Fig. S4 (b). Cutting across this center we use a Gaussian fit ($C_I(\mathbf{r}) \propto e^{-|\mathbf{r}|^2/(2\sigma_c^2)}$) to extract the correlation length, σ_c as the standard deviation of the fitted Gaussian, depicted in Fig S4 (c). We change the speckle size by moving lens L1 closer or further away from the diffuser, keeping the diffuser at a fixed distance from the cell. This allows us to keep the width of the Gaussian envelope of the beam approximately constant, while at the same time changing the speckle size.

As discussed above, the choice of a central AOI is important in the analysis of our data. Whereas it is favourable to have larger AOIs to have include larger number of speckle grains yielding better statistics, the size of the AOI is limited by the size of the Gaussian envelope of the beam. The AOI should be a sufficiently small central area of the beam such that the Gaussian envelope is not affecting the statistics and nonlinear propagation. A good criterion was found to have the intensity histogram for a far detuned beam well described by an exponential, an example of which is shown in Fig. 2. For a a AOI that is too large the number of low intensity pixels in the wings of the Gaussian envelope will increase and the distribution will cease to be exponential. Similarly, for a AOI that is too small the number of low intensity pixels will decrease, also resulting in deviations from the expected exponential intensity distribution.

Initial increase of precondensate fraction

We consider that the initial speckle field is characterized by Gaussian fluctuations that are statistical homogeneous in space $\psi(z = 0, \mathbf{r}) = \psi_0(\mathbf{r})$ with a correlation function

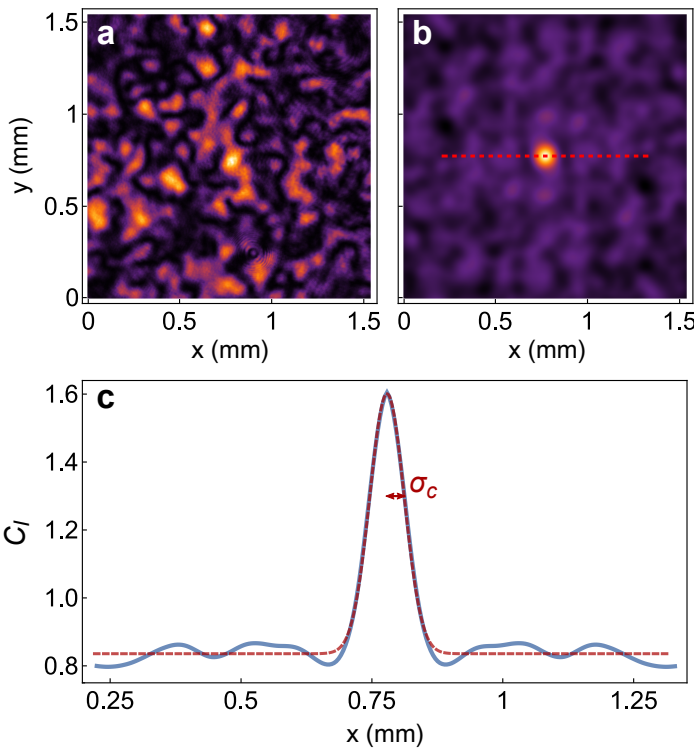


FIG. S4: Calibration of the correlation length. (a) An example of a near field image of the speckle field. (b) The corresponding calculated 2D correlation function. The red dashed line indicates the line shown in (c) used to extract the correlation length fit σ_c . (c) The experimental data (blue, full line) and the fitted Gaussian distribution (red, dashed line).

$C_0(\mathbf{r}) = \langle \psi_0(\mathbf{r}' + \mathbf{r})\psi_0^*(\mathbf{r}') \rangle$ of the form $I_0 \exp(-|\mathbf{r}|^2/(4\sigma_c^2))$, where σ_c is the correlation length of the intensity distribution of the incident speckle [$C_I(\mathbf{r}) \propto \exp(-|\mathbf{r}|^2/(2\sigma_c^2))$] and $C_0(0) = I_0 = \langle |\psi_0(\mathbf{r})|^2 \rangle$ is the mean intensity. When absorption can be neglected, the mean intensity $\langle I \rangle$ and the mean Hamiltonian $\langle H \rangle$ are preserved: $\langle I \rangle = \langle |\psi(z, \mathbf{r})|^2 \rangle$, $\langle H \rangle = \langle E \rangle(z) + \langle U \rangle(z) = \frac{1}{2k_0} \langle |\nabla \psi(z, \mathbf{r})|^2 \rangle + \frac{\gamma}{2} \langle |\psi(z, \mathbf{r})|^4 \rangle$. At $z = 0$, the mean kinetic energy is $\langle E \rangle_0 = -\frac{1}{2k_0} \nabla^2 C_0(0)$, while the mean nonlinear energy is $\langle U \rangle_0 = \gamma I_0^2$. Considering the example of a Gaussian-shaped correlation function, the ratio between the linear and nonlinear energies is given by:

$$\frac{\langle E \rangle_0}{\langle U \rangle_0} = \left(\frac{\Lambda}{\sigma_c} \right)^2 \quad (\text{S5})$$

It is also interesting to note that, normalizing the spatial variable (\mathbf{r}) with respect to the healing length Λ and $|\psi|^2$ with respect to I_0 , the dimensionless initial kinetic energy reads $\langle \tilde{E} \rangle_0 = (\Lambda/\sigma_c)^2$, and the dimensionless initial nonlinear energy $\langle \tilde{U} \rangle_0 = 1$. Accordingly, the conserved dimensionless Hamiltonian is fixed by the initial condition:

$$\langle \tilde{H} \rangle = \left(\frac{\Lambda}{\sigma_c} \right)^2 + 1, \quad (\text{S6})$$

which shows again the relevance of the parameter $(\Lambda/\sigma_c)^2$. As discussed in the main text through Eq.(2), the precondensate fraction, n_0/I_0 , is related to the variance of intensity

fluctuations. At $z = 0$ we have $\langle |\psi_0(\mathbf{r})|^4 \rangle / \langle |\psi_0(\mathbf{r})|^2 \rangle^2 = 2$.

- *Strong nonlinear regime:* In the regime $\langle U \rangle > \langle E \rangle$, i.e. $\gamma I_0 > (2k_0)^{-1} \sigma_c^{-2}$, we can consider the diffraction term as a perturbation. To leading order we have $\psi(z, \mathbf{r}) = \psi_0(\mathbf{r}) \exp(-i\gamma|\psi_0(\mathbf{r})|^2 z)$, and therefore the correlation function of the field $C(z, \mathbf{r}) = \langle \psi(z, \mathbf{r}' + \mathbf{r})\psi^*(z, \mathbf{r}') \rangle$, is $C(z, \mathbf{r}) = C_0(\mathbf{r}) / [1 + B^2(z)(1 - C_0^2(\mathbf{r})/C_0^2(0))]^2$, with $B(z) = \gamma C_0(0)z$ the mean cumulative nonlinear phase. The kinetic energy therefore evolves as $\langle E \rangle(z) = -\frac{1}{2k_0} \nabla^2 C_0(0)[1 + 4B^2(z)]$. By conservation of the mean Hamiltonian, we can deduce:

$$\frac{\langle I(z, \mathbf{r})^2 \rangle}{I_0^2} = 2 + 4\nabla^2 C_0(0)\gamma z^2/k_0 + o(z^2). \quad (\text{S7})$$

This result is valid as long as $|\nabla^2 C_0(0)|\gamma z^2/k_0 < 1$.

- *Expansion for small propagation lengths:* Another approach consists in expanding the field $\psi(\mathbf{r}, z)$ for small z . Here we take into account a possible saturation of the nonlinearity and denote $\varrho(\mathbf{r}) = 1/(1 + \alpha|\psi_0|^2(\mathbf{r}))$. Expanding the field up to $o(z^2)$, $\psi(z, \mathbf{r}) = \psi_0(\mathbf{r}) + z\psi_1(\mathbf{r}) + z^2\psi_2(\mathbf{r}) + o(z^2)$, it can be shown that: $\langle |\psi|^4 \rangle = \langle |\psi_0|^4 \rangle + z^2 \{ 4\langle |\psi_0|^2|\psi_1|^2 \rangle + 2\text{Re}(\langle \psi_0^2\psi_1^{*2} \rangle) + 2\text{Re}(\langle |\psi_0|^2\psi_2\psi_0^* \rangle) \} + o(z^2)$. Straightforward calculations using the Gaussian summation rule for high-order moments and the fact that $\nabla\psi_0(\mathbf{r})$ and $\psi_0(\mathbf{r})$ are independent give $\langle |\psi|^4 \rangle = 2C_0(0)^2 + 2k_0^{-1}\nabla^2 C_0(0)Q(\alpha C_0(0))\gamma C_0(0)^2 z^2 + o(z^2)$, where $Q(y) = \int_0^\infty \frac{s^2 - ys^3}{(1+ys)^3} e^{-s} ds$, which can be expanded for small y as $Q(y) = 2 - 24y + O(y^2)$. Therefore we obtain:

$$\frac{\langle I(z, \mathbf{r})^2 \rangle}{I_0^2} = 2 + \frac{2\nabla^2 C_0(0)Q(\alpha C_0(0))\gamma z^2}{k_0} + o(z^2). \quad (\text{S8})$$

When $\alpha C_0(0) \ll 1$ (i.e., the saturable nonlinearity can be neglected) we recover the same result as in Eq.(S7). This result is obtained by assuming that $|\nabla^4 C_0(0)|z^2/[k_0^2 C_0(0)]$ and $\gamma^2 C_0(0)^2 z^2$ are smaller than one.

- *Precondensate fraction:* For a Gaussian-shaped correlation function $C_0(\mathbf{r}) = I_0 \exp(-|\mathbf{r}|^2/(4\sigma_c^2))$, i.e., $|\nabla^2 C_0(0)| = I_0/\sigma_c^2$, Eq.(S7) [or Eq.(S8) with $\alpha I_0 \ll 1$] leads to

$$\frac{n_0}{I_0} = 2\sqrt{2} \frac{\Lambda}{\sigma_c} \frac{z}{z_{NL}} + o(z), \quad (\text{S9})$$

where we have used $n_0/I_0 = \sqrt{2 - \langle I^2 \rangle / I_0^2}$. This expression has been found in quantitative agreement with the simulations (see dark-dashed line in Fig. 4(a) in the main text).

Precondensation vs thermalization

A refined analysis of the precondensation process reveals that it occurs in two stages. In the first stage $z \lesssim z_{NL}$, the precondensate fraction exhibits the sudden growth described by (S9), which is characterized by an energy transfer between the kinetic (E) and nonlinear (U) contributions, see Fig. S6(a). Notice that, by energy conservation, the evolution of the fourth-order moment of the field (nonlinear contribution to the Hamiltonian), can be related to the rate of change of the width of the spectrum (linear contribution to the Hamiltonian) [7]. In our case, the nonlinear energy is related to the precondensate amplitude, then we have

$$\frac{\langle E \rangle(z)}{\gamma I_0^2} = \frac{1}{2} \frac{n_0^2(z)}{I_0^2} - 1 + \frac{\langle H \rangle}{\gamma I_0^2}. \quad (\text{S10})$$

This first stage is characterized by the population of high-frequency components, while the low frequency part of the spectrum remains almost invariant, as illustrated in Fig. S6(c-d). In the second stage (typically $z_{NL} \lesssim z \lesssim 200z_{NL}$), the part of the spectrum nearby $k \sim \Lambda^{-1}$ exhibits a bi-directional redistribution, with particles (power) transferred toward the low- and high-frequency components, i.e., particles flow toward the coherent precondensate component ($\psi_c(\mathbf{r})$ for $k < \Lambda^{-1}$) and the incoherent component ($\phi(\mathbf{r})$ for $k > \Lambda^{-1}$), see Eq.(S12). In this second stage, the kinetic energy and the precondensate fraction reach their (asymptotic) thermal equilibrium values for $z \gtrsim 200z_{NL}$, see Fig. S6(b).

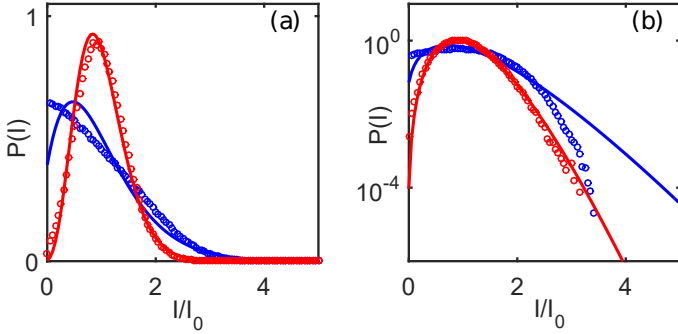


FIG. S5: 1D vs 2D systems. Comparison of the probability density functions for the integrable 1D NLS equation (blue lines and blue circles), and the 2D NLS equation (red lines and red circles), in normal scale (a), and logarithmic scale (b). The circles denote the results of NLS simulations, the lines the theoretical probability density function given by Eq.(2) (main text) where the parameter n_0 is computed from the variance of intensity fluctuations. For the integrable 1D case, the spectral evolution of the wave does not exhibit an accumulation of particles to $k = 0$, so that the probability densities $P(I)$ are of different nature in 1D and 2D, in both the core of the distribution (a), and the corresponding tail (b): At variance with the good agreement between theory and simulations in 2D, the 1D probability density is not of the form predicted by the theory of precondensation (Eq.(2) in the main text). The same value of the Hamiltonian has been considered in 1D and 2D, $\tilde{H} = 1.7$, at $z = 10^4 z_{NL}$.

This fast prethermalization process of E and n_0 is in marked contrast with the slow dynamical thermalization of the spectrum toward the Rayleigh-Jeans equilibrium state. Indeed, such a slow thermalization requires propagation lengths several order of magnitudes larger, $z \gtrsim 10^5 z_{NL}$. This is revealed by the evolution of the spectrum (see Fig. S6(c)), or by the evolutions of the modal components $n_{k_j}(z) \propto |\tilde{\psi}|^2(k_j, z)$ (see Fig. S6(d)) and in particular the zero-momentum condensate $n_0^{\text{FF}}(z) \propto |\tilde{\psi}|^2(k = 0, z)$ (see blue lines in panels (b) and (d) of Fig. S6).

The nonequilibrium nature of the process of precondensation is also revealed through the analysis of the first-order correlation functions of the near field. Indeed, at equilibrium, the 2D NLS equation is known to exhibit a Berezinskii-Kosterlitz-Thouless phase in the strong condensation regime [8]. In this equilibrium regime, the completely thermalized state of the 2D NLS equation is characterized by a power-law tail of the correlation function. We computed the normalized correlation function at different propagation lengths

$$g_1(z, \mathbf{r}) = \frac{C(z, \mathbf{r})}{I_0}. \quad (\text{S11})$$

The results are reported in Fig. S7, which shows that during the whole process of precondensation the correlation function exhibits a fast decay (see red and green crosses). In contrast, long-range order is eventually established at thermal equilibrium (see blue crosses for $z = 150 \times 10^3 z_{NL}$) where $g_1(r) \sim r^{-\nu}$ with $\nu \simeq 0.025$ (dashed red line).

Notice that both fast precondensation and slow thermalization processes are not properly described by a weakly nonlinear approach. Indeed, precondensation takes place in the nonlinear regime ($\langle E \rangle_0 < \langle U \rangle_0$), and at thermal equilibrium ($z > 10^5 z_{NL}$) the kinetic energy $\langle E \rangle_{eq}$ is of the same order as the nonlinear energy $\langle U \rangle_{eq}$, see Fig. S6(a). In the context of non-thermal fixed points [9], the spectra of inverse cascades predicted in the strongly nonlinear regime are characterized by steep power-law spectra in the far infrared region (very small k). The formation of such anomalous power-law spectra are known to require an initial strong cooling quench, which is featured by a specific initial momentum distribution. For this reason they have not been identified in our simulations, since we start our simulations from the conventional speckle-like Gaussian spectrum considered in the experiments, see Fig. S6(c). It is interesting to remark in Fig. S6(b) that a significant growth of $n_0^{\text{FF}}(z)$ occurs for $z \gtrsim 200z_{NL}$, once the kinetic energy E and the precondensate fraction n_0 have already reached their thermalized equilibrium values.

We note that the sudden variation of the precondensate fraction in Eq.(S9) is a phenomenon driven by nonlinear effects, so that it occurs irrespective of the dimensionality of the problem. Accordingly, purely one-dimensional systems can exhibit an apparent similar effect [10–13]. However, the phenomenology of ‘integrable turbulence’ in 1D is of fundamental different nature than the 2D case discussed here. Indeed, the integrable 1D NLS equation does not exhibit neither thermalization to the Rayleigh-Jeans distribution, nor the accumulation of ‘particles’ toward $k = 0$ [14–16]. This has a deep consequence on the probability density functions: The distributions cannot be of the form given in Eq.(2) in the main text, which implicitly assumes the presence of a pre-condensate of amplitude $\sqrt{n_0}$ (i.e., $\psi(\mathbf{r}) = \sqrt{n_0} + \phi(\mathbf{r})$). This aspect is clearly illustrated in Fig. S5, which evidences the different nature of 1D and 2D probability densities, in both the core and the tail of the distribution. Notice in particular that the probability distribution predicted in the theory of precondensation (given in Eq.(2) of the main text) is not consistent with 1D simulations (see blue lines and blue circles in Fig. S5).

We note that the parameters used in the simulations reported in Fig. S6 correspond to those of Fig. 4 in the main text: We used 512^2 modes with a numerical window of $L_{\text{num}} = 256\Lambda$, which is of the order of the size of the beam used in the experiments. The energy of the initial conditions in Fig. 4 is $\tilde{H} = 1 + (\Lambda/\sigma_c)^2 = 1.69$. Periodic boundary conditions have been used by considering an initial random wave with homogeneous spatial fluctuations, as in the theory developed above. The initial random wave is characterized by a Gaussian spectrum with uncorrelated random spectral phases.

Robustness of the notion of precondensation

- *Multimode nonequilibrium intensity distribution:* As discussed in the main text, the conventional decomposition of the field $\psi(\mathbf{r}, z) = \sqrt{n_0} + \phi(\mathbf{r}, z)$ can be refined to describe

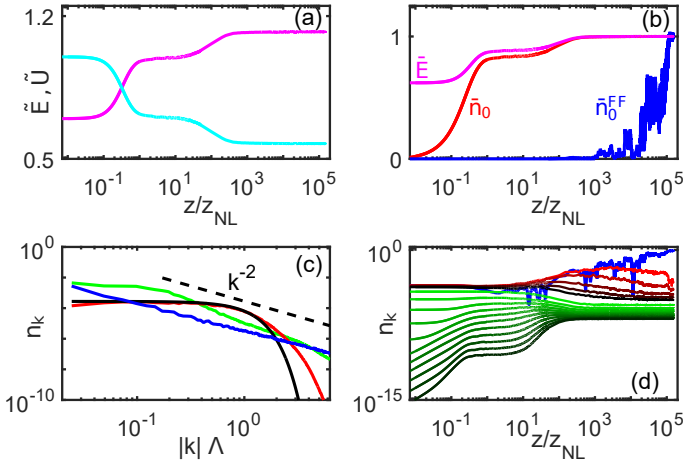


FIG. S6: Precondensation vs thermalization. Numerical simulation of the NLS Eq.(1) (in the main text). (a) Evolutions of the normalized kinetic energy \tilde{E} (magenta line) and nonlinear energy \tilde{U} (light blue line) – note the \log_{10} -scale evolution in the z -axis. (b) Evolutions of the kinetic energy $\bar{E}(z) = E(z)/E^{eq}$ (magenta line), precondensate $\bar{n}_0(z) = n_0(z)/n_0^{eq}$ (red line), zero-momentum condensate $\bar{n}_0^{FF}(z) = n_0^{FF}(z)/n_0^{FF,eq}$ (blue line): The evolutions have been normalized with respect to their equilibrium values at $z \gtrsim 150 \times 10^3 z_{NL}$. (c) Spectra of the field vs $k = |\mathbf{k}|$ at $z = 0$ (black line), $z = z_{NL}$ (red line), $z = 100z_{NL}$ (green line), $z = 10^5 z_{NL}$ (blue line), in log-log-scale. The black dashed line shows the Rayleigh-Jeans power law behavior $\sim k^{-2}$. (d) Evolutions during the propagation z of the modal components $n_{k_j}(z)$ (from top to bottom at $z = 1.5 \times 10^5 z_{NL}$): $k = 0$, $k = 2$, $k = 5$, $k = 10$, $k = 15$ and then $k_j = j\Delta_k$, $j = 1, \dots, 12$ with $\Delta_k = 20$ (k and Δ_k being in units of the fundamental frequency interval $2\pi/L_{num}$), in log-log-scale. Note that for each k_j , $n_{k_j}(z) \simeq \text{const}$ for $z \gtrsim 1.1 \times 10^5 z_{NL}$. Parameters are the same as in Fig. 4 (main text): The size of the numerical window is $L_{num} = 256\Lambda$, with 512^2 modes; the statistics of the initial random wave $\psi_0(\mathbf{r})$ is homogeneous in space, with the energy $\tilde{H} = 1.69$.

the effect of precondensation. We assume that the random field with mean intensity I_0 can be decomposed in the form

$$\psi(\mathbf{r}, z) = \psi_c(\mathbf{r}, z) + \phi(\mathbf{r}, z), \quad (\text{S12})$$

where ψ_c is the coherent slowly-varying precondensate component, while $\phi(\mathbf{r}, z)$ is still the incoherent rapidly-varying field that exhibits Gaussian statistics. The coherent component evolves in the nonlinear regime, so that the intensity distribution $p_{I_c}(I_c)$ of the coherent component $I_c = |\psi_c|^2$ is not known in analytic form and is computed numerically by filtering the low-frequency part of the spectrum, $k \in [0, k_{coh}]$, with $k_{coh} \simeq 1/\Lambda$. In the ultimate regime where full thermalization is achieved, the coherent field is a pure homogeneous plane-wave, $p_{I_c}(I_c) = \delta(I_c - n_0)$. Far from equilibrium, we can define the precondensate component by $\langle I_c \rangle = \int_0^\infty I_c p_{I_c}(I_c) dI_c$. The intensity distribution of the whole intensity $I = |\psi|^2$ can be written as the mixture:

$$P_I(I) = \int_0^\infty p_{I|I_c}(I|I_c) p_{I_c}(I_c) dI_c, \quad (\text{S13})$$

where $p_{I|I_c}(I|I_c) = J_0^{-1} \exp(- (I + I_c)/J_0) \mathcal{I}_0(2\sqrt{I_c I}/J_0)$ denotes the conditional distribution function given that the

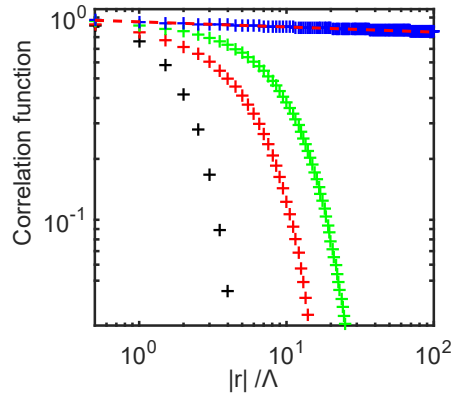


FIG. S7: Analysis of the correlation function. First-order correlation function $g_1(z, \mathbf{r})$ [see Eq.(S11)] as a function of an angle-averaged distance $r = |\mathbf{r}|$ in a log-log plot. The correlation function $g_1(z, \mathbf{r})$ is computed at different propagation lengths: $z = 0$ (black), $z = 60z_{NL}$ (red), $z = 200z_{NL}$ (green), $z = 150 \times 10^3 z_{NL}$ (blue). During the whole process of precondensation ($z \lesssim 200z_{NL}$) the correlation function exhibits a fast decay. In contrast, long-range order is eventually established at thermal equilibrium (see blue crosses) where the correlation function exhibits a power-law decay, $g_1(r) \sim r^{-\nu}$ (dashed red line). Parameters are the same as in Fig. S6: The size of the numerical window is $L_{num} = 256\Lambda$, with 512^2 modes; the statistics of the initial random wave $\psi_0(\mathbf{r})$ is assumed homogeneous in space, with the energy $\tilde{H} = 1.69$.

intensity of the coherent component is I_c , while $J_0 = I_0 - \langle I_c \rangle$ is the average intensity of the incoherent (statistically Gaussian) component. Note in particular that if $p_{I_c}(I_c) = \delta(I - I_c)$ then the present definition of $n_0 = \langle I_c \rangle$ coincides with the previous one defined through the distribution given by Eq.(2) in the main text. We remark that the variances are related by:

$$\text{Var}(I) = \text{Var}(I_c) + I_0^2 - \langle I_c \rangle^2. \quad (\text{S14})$$

If $\text{Var}(I_c) = \langle I_c^2 \rangle - \langle I_c \rangle^2 = 0$ (i.e., $p_{I_c}(I_c) = \delta(I_c - n_0)$ and $\langle I_c \rangle = n_0$), then

$$\langle I_c \rangle = \sqrt{2I_0^2 - \langle I^2 \rangle}. \quad (\text{S15})$$

In general we have $\text{Var}(I_c) > 0$, then $\langle I_c \rangle > n_0$ and

$$\langle I_c \rangle = \sqrt{2I_0^2 - \langle I^2 \rangle + \text{Var}(I_c)}. \quad (\text{S16})$$

We report in Fig. S8(a) the intensity distributions obtained from Eq.(2) (in the main text) and Eq.(S13), as well as the intensity distributions obtained by the numerical simulation reported in Fig. 4 (main text) for $z = 100z_{NL}$. The comparison indicates that the bare intensity distribution Eq.(2) is well corroborated by the generalized intensity distribution (S13) that accounts for the multimode nature of the precondensate. Note however that, as expected, the generalized intensity distribution (S13) is quite sensitive to the low-frequency cut-off (k_{coh}) that defines the coherent component, ψ_c (we identified in particular some deviations from Gaussian statistics for the incoherent component even for $k_{coh} = 1.5\Lambda^{-1}$ considered in Fig. S8).

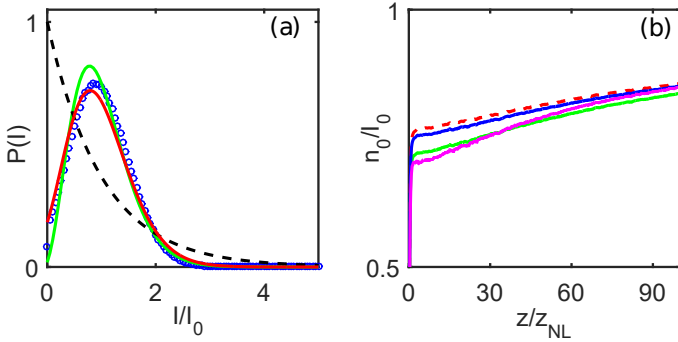


FIG. S8: **Robustness of the precondensate.** (a) Probability densities of the intensity $|\psi|^2$, obtained from the monomode model Eq.(2) in the main text (green line), and multimode model Eq.(S13) (red line). The blue circles denote the corresponding intensity distribution obtained by the simulation reported in Fig. 4 in the main text for $z = 100z_{NL}$. The dark-dashed line refers to the intensity distribution of $|\psi|^2$ at $z = 0$ (Gaussian statistics). (b) Evolution of the precondensate fraction n_0/I_0 vs. z computed from different moments of the intensity $\langle I^p \rangle$, as given by Eqs.(S18-S19): $p = 2$ (blue), $p = 1.5$ (red), $p = 0.5$ (green). The magenta line is obtained by fitting the numerical results to the probability density given in Eq.(2) in the main text. Parameters are the same as in Fig. 4 (main text): The size of the numerical window is $L_{num} = 256\Lambda$, with 512^2 modes; the statistics of the initial random wave $\psi_0(\mathbf{r})$ is assumed homogeneous in space, with the energy $\tilde{H} = 1.69$.

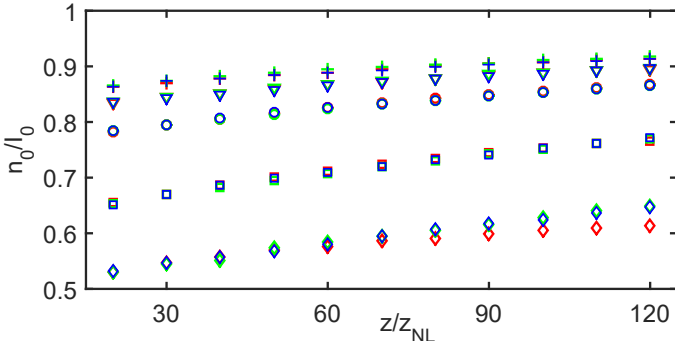


FIG. S9: **Robustness with respect to the frequency cut-off.** Evolution during the propagation of the precondensate fraction n_0/I_0 obtained by simulations of the NLS Eq.(1) (in the main text) for different values of the frequency cut-off: $k_c = 2\pi\Lambda^{-1}$ (red), $k_c = 4\pi\Lambda^{-1}$ (green), $k_c = 8\pi\Lambda^{-1}$ (blue); and different values of the normalized Hamiltonian, $\tilde{H} = 6$ (\diamond), $\tilde{H} = 3.25$ (\square), $\tilde{H} = 1.7$ (\circ), $\tilde{H} = 1.3$ (∇), $\tilde{H} = 1$ (+). The precondensate proves robust with respect to variations of k_c . The system size is kept fixed, $L_{num} = 256\Lambda$.

- *Generalized moment computation of n_0/I_0 :* The standard estimation of the precondensate n_0 from the intensity distribution of Eq.(2) (in the main text) is based on the second-order moment of the intensity, $n_0 = \sqrt{2I_0^2 - \langle I^2 \rangle}$. It is important to note that n_0 can also be estimated from different moments of the intensity. We find that, for any $p > 0$

$$\frac{\langle I^p \rangle}{I_0^p} = \mathcal{F}_p\left(\frac{n_0}{I_0}\right), \quad (\text{S17})$$

where

$$\mathcal{F}_p(x) = e^{-\frac{x}{1-x}}(1-x)^p \Gamma(1+p) M_K\left(1+p, 1, \frac{x}{1-x}\right). \quad (\text{S18})$$

In this expression, $\Gamma(x)$ is the gamma function, while M_K is the Kummer's function, which is a particular confluent geometric function, see [19]. By inverting this expression, we can extract n_0/I_0 from $\langle I^p \rangle$ (for $p \neq 1$):

$$\frac{n_0}{I_0} = \mathcal{F}_p^{-1}\left(\frac{\langle I^p \rangle}{I_0^p}\right), \quad (\text{S19})$$

\mathcal{F}_p^{-1} being the inverse function of \mathcal{F}_p . We report in Fig. S8(b) the evolutions of the condensate fractions computed with different values of the intensity moments. Note that the moment with $p = 1/2$ is less sensitive to the tail of the intensity distribution than $p = 1.5$ or $p = 2$. We remark in Fig. S8(b) that the precondensate fraction is almost insensitive to the choice of the particular moment. We have also computed n_0/I_0 from a direct fit to Eq.(2) in the main text, which is found in agreement with the moment estimations, see magenta line in Fig. S8(b). This analysis corroborates the validity of the simple model based on the intensity probability distribution given in Eq.(2) in the main text.

- *Influence of the frequency cut-off:* Ensembles of classical waves exhibit the well-known ultraviolet catastrophe, which is regularized by the introduction of an arbitrary frequency cut-off (k_c) in the spectrum [16]. At variance with the usual equilibrium zero-momentum condensation (n_0^{FF}), precondensation does not require the introduction of a frequency cut-off, because it occurs very far from thermal equilibrium. We report in Fig. S8(b) the evolution of the precondensate fraction n_0/I_0 for different values of the frequency cut-off that regularizes the ultraviolet catastrophe inherent to ensemble of classical waves. The frequency cut-off, $k_c = \pi/dx$, arises in the simulations because of the spatial discretization (dx) of the NLS equation. As illustrated in Fig. S9, the simulations reveal that, whenever $k_c \gtrsim 2\pi\Lambda^{-1}$ (i.e., the healing length Λ is discretized by at least two points), the precondensate fraction is almost independent of the frequency cut-off. Indeed, for moderate propagation lengths available in the experiment ($z \sim 100z_{NL}$), the power-law tail of the Rayleigh-Jeans distribution $\sim k^{-2}$ is not yet established and higher-order modes are only weakly populated. Also note that the thermalization length is sensitive to the size of the numerical window L_{num} .

- *Robustness with respect to non-Gaussian initial statistics:* In the main text we have considered initial random waves characterized by a Gaussian statistics. Here we study by numerical simulations the impact of a non-Gaussian initial statistics. We have shown that the probability density relaxes during the evolution toward the low-tailed distribution given by Eq.(2) (in the main text). Hence, here we test the relaxation process by considering an initial condition featured by a heavy-tail probability density:

$$P(I) = \frac{\exp(-\sqrt{2I/I_0})}{\sqrt{2II_0}}, \quad (\text{S20})$$

where $I_0 = \langle I \rangle$ still denotes the average intensity. As illustrated in Fig. S10(a), this density is featured by a heavy-tail in the sense that the tail of the distribution

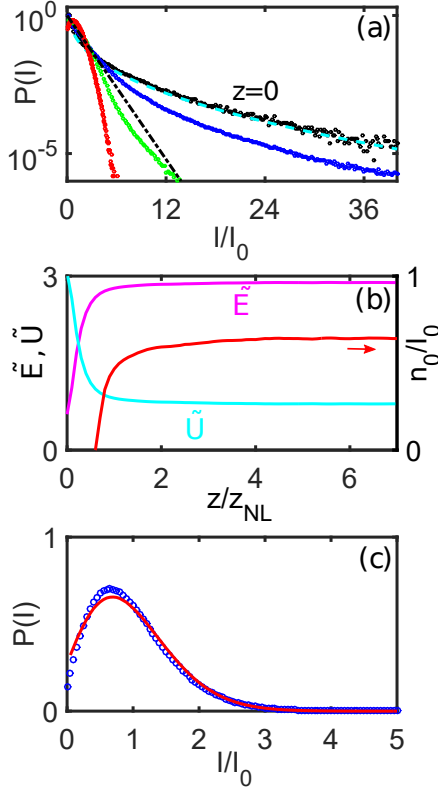


FIG. S10: Robustness of precondensation with non-Gaussian initial statistics. (a) Evolution of the probability density of the random wave: initial condition at $z = 0$ (black dots), $z = z_{NL}$ (blue dots), $z = 2z_{NL}$ (green dots), $z = 200z_{NL}$ (red dots). The dashed cyan line refers to the analytical expression of $P(I)$ given in Eq.(S20), the dashed black line denotes the Gaussian distribution. (b) Evolutions of the kinetic energy \tilde{E} (magenta line), nonlinear energy \tilde{U} (blue line), and precondensate fraction n_0/I_0 (red line). (c) Probability density of the wave at $z = 200z_{NL}$ (blue circles) and corresponding theoretical expression given by Eq.(2) in the main text (red line). The normalized energy is $\tilde{H} = 3.67$.

is above the Gaussian statistics (dashed cyan line in Fig. S10(a)). During the propagation of the incoherent wave the heavy-tail probability density rapidly relaxes toward a low-tail distribution. This process is characterized by an exchange of linear and nonlinear energies (see Fig. S10(b)), in a way analogous to the case studied above with initial Gaussian statistics. Note that, because of the initial heavy-tail distribution, the incoherent wave exhibits a large variance of intensity fluctuations, $\langle I^2 \rangle(z=0) = 6I_0^2$, so that the precondensate fraction defined from the second-order moment ($n_0/I_0 = \sqrt{2 - \langle I^2 \rangle/I_0^2}$) is not defined, which explains the delay in the growth of n_0/I_0 in Fig. S10(b). Next, because the variance rapidly decreases during the propagation, n_0/I_0 exhibits a rapid linear growth and then saturates to a quasi-steady state, as in the case of initial Gaussian statistics considered above. This is confirmed by the good agreement that we have found between the statistics of the random wave and the corresponding theoretical prediction of the probability density given by Eq.(2) (in the main text). This numerical study shows that the precondensation effect is robust with respect to deviations from Gaussianity of the initial random wave.

- *Influence of a nonlocal nonlinearity:* Light propagation in atomic vapours can be affected by the nonlocal property of the nonlinearity [20]. In general, a nonlocal nonlinearity is modelled by a kernel in the nonlinear term of the NLS equation:

$$i \frac{\partial \psi}{\partial z} = -\frac{1}{2k_0} \nabla^2 \psi + \gamma \int V(|\mathbf{r} - \mathbf{r}'|) |\psi|^2(\mathbf{r}') d\mathbf{r}', \quad (\text{S21})$$

where the width of the response function $V(\mathbf{r})$, say ζ , denotes the range of nonlocality ($\int V(\mathbf{r}) d\mathbf{r} = 1$). Using the excited state population decay as an indicator for nonlocality, this gives an exponential-shaped nonlocal function $V(r)$ [20]. We report in Fig. S10(a) numerical simulations of the nonlocal NLS (S21) for different values of the nonlocal range ζ . Globally, the impact of nonlocality is to reduce the initial growth of the precondensate fraction, as well as its subsequent saturation to a quasi-stationary value. We also remarked that simulations with a large value of the nonlocal range can capture some features observed in the experiment, such as a delay in the initial growth of n_0/I_0 , see Fig. S10(a). We report in Fig. S10(b) the precondensate fraction n_0/I_0 vs $(\Lambda/\sigma_c)^2$ for different values of the nonlocal parameter ζ . We can notice that for small correlation lengths σ_c (large values of $(\Lambda/\sigma_c)^2$), the spatial range of nonlocality involves several speckles ($\zeta \gtrsim \sigma_c$), which deeply impacts the dynamics and leads to a significant dispersion of the precondensation curves for small n_0/I_0 . On the other hand, when $\zeta \lesssim \sigma_c$ the nonlocal range typically gets smaller than the coherence length (for small $(\Lambda/\sigma_c)^2$), so that nonlocality only weakly affects the dynamics, thus leading to a collapse of the precondensation curves for large n_0/I_0 . This could explain the origin of the dispersion of the different curves of precondensation reported in the experiment for small n_0/I_0 , see Fig. 3(b) in the main text (note however that in the simulations we computed n_0/I_0 at $z = 80z_{NL}$, while in the experiments the nonlinear coefficient γ is varied keeping constant the propagation length of the sample L). A more detailed analysis of nonlocality on the effect of precondensation in atomic vapours will be the subject of further studies. We also note that wave condensation at equilibrium in the presence of nonlocality has been studied theoretically in Ref. [21].

- *Weak vs strong nonlinear regime:* In the weakly nonlinear regime, $\langle E \rangle_0 \gg \langle U \rangle_0$, or $(\Lambda/\sigma_c)^2 \gg 1$, the weak turbulence theory applies and one does not expect precondensation since the kinetic energy is conserved during propagation, although in practice small deviations from Gaussian statistics lead to a non-vanishing precondensate fraction n_0/I_0 . In this regime, n_0/I_0 deviates significantly from the equilibrium condensate fraction, although such an equilibrium condensate strongly depends on the arbitrary choice of the frequency cut-off [16].

In the opposite regime of strong nonlinear interaction, $\langle E \rangle_0 \ll \langle U \rangle_0$, or $(\Lambda/\sigma_c)^2 \ll 1$ and $n_0/I_0 \sim 1$, very different features appear. In this regime, one expects the formation of shock waves from the initial incoherent field [17, 18]. The regularization of the shock singularities is characterized by the formation of rapid oscillations ('undular bores') on the healing length scale $\sim \Lambda$. The spectrum then evidences the population of modes near $k \sim \Lambda^{-1}$, so that the initial population of $k \sim 0$ can decrease, before increasing again to reach the steady state precondensate fraction, n_0/I_0 .

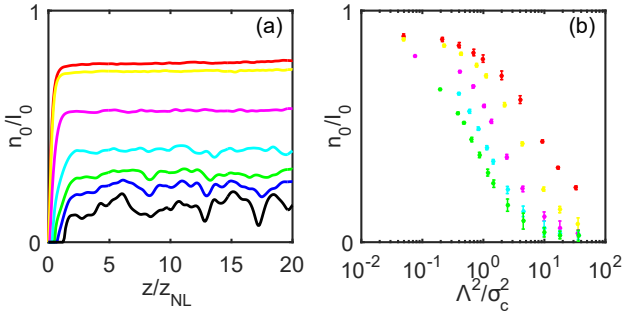


FIG. S11: Robustness with respect to nonlocality. (a) Evolution of the precondensate fraction n_0/I_0 obtained by simulations of the nonlocal NLS Eq.(S21) for different values of the nonlocal range ζ ; (b) precondensate fraction n_0/I_0 at $z = 80z_{NL}$ vs $(\Lambda/\sigma_c)^2$ for different ζ . from top to bottom, local limit $\zeta = 0$ (red), $\zeta = 0.2\Lambda$ (yellow), $\zeta = \Lambda$ (magenta), $\zeta = 3\Lambda$ (cyan), $\zeta = 6\Lambda$ (green), $\zeta = 10\Lambda$ (blue), $\zeta = 30\Lambda$ (black) (the frequency cut-off is $k_c = 4\pi$). Note in (b) that the different curves of precondensation tend to collapse for large n_0/I_0 (small $(\Lambda/\sigma_c)^2$).

- [1] Y. Wang, M. Saffman, Experimental study of nonlinear focusing in a magneto-optical trap using a Z-scan technique, Phys. Rev. A **70**, 013801 (2004).
- [2] Y. R. Shen, The Principles of Nonlinear Optics, New York: J. Wiley (1984)
- [3] F. Simoni, Nonlinear Optical Properties of Liquid Crystals and Polymer Dispersed Liquid Crystals, World Scientific (1997).
- [4] G.P. Agrawal, Nonlinear Fiber Optics, Academic Press (2013).
- [5] L. Deng, K. He, T. Zhou and C. Li, Formation and evolution of far-field diffraction patterns of divergent and convergent Gaussian beams passing through self-focusing and self-defocusing media J. Opt. A: Pure Appl. Opt. **7**, 409-415 (2005)
- [6] E. V. Garcia Ramirez, M. L. Arroyo Carrasco, M. M. Mendez Otero, S. Chavez Cerda, and M. D. Iturbe Castillo, Far field intensity distributions due to spatial self phase modulation of a Gaussian beam by a thin nonlocal nonlinear media Opt. Express **18**, 22067-22079 (2010)
- [7] M. Onorato, D. Proment, G. El, S. Randoux, P. Suret, On

the origin of heavy-tail statistics in equations of the Nonlinear Schrödinger type, Phys. Lett. A **380**, 3173 (2016).

- [8] S. Nazarenko, M. Onorato, and D. Proment, Bose-Einstein condensation and Berezinskii-Kosterlitz-Thouless transition in the two-dimensional nonlinear Schrödinger model, Phys. Rev. A **90**, 013624 (2014).
- [9] B. Nowak, S. Erne, M. Karl, J. Schole, D. Sexty, and T. Gasenzer, Non-thermal fixed points: universality, topology & turbulence in Bose gases, in *Strongly Interacting Quantum Systems out of Equilibrium*, edited by T. Giamarchi, A. Millis, O. Parcollet, H. Saleur, L. Cugliandolo (2013).
- [10] J. Berges, T. Gasenzer, Quantum versus classical statistical dynamics of an ultracold Bose gas, Phys. Rev. A **76**, 033604 (2007).
- [11] Y. Bromberg, Y. Lahini, E. Smalland, Y. Silberberg, Hanbury Brown and Twiss interferometry with interacting photons, Nature Photonics **4**, 721 (2000).
- [12] Y. Silberberg, Y. Lahini, Y. Bromberg, E. Small, and R. Morandotti, Universal Correlations in a Nonlinear Periodic 1D System, Phys. Rev. Lett. **102**, 233904 (2009).
- [13] S. Randoux, P. Walczak, M. Onorato, P. Suret, Nonlinear random optical waves: Integrable turbulence, rogue waves and intermittency, Physica D **333**, 323 (2016).
- [14] P. Walczak, S. Randoux, and P. Suret, Optical Rogue Waves in Integrable Turbulence, PRL **114**, 143903 (2015).
- [15] J.M. Soto-Crespo, N. Devine, N. Akhmediev, Integrable Turbulence and Rogue Waves: Breathers or Solitons?, Phys. Rev. Lett. **116**, 103901 (2016).
- [16] A. Picozzi, J. Garnier, T. Hansson, P. Suret, S. Randoux, G. Millot, D. Christodoulides. Optical wave turbulence: Toward a unified nonequilibrium thermodynamic formulation of statistical nonlinear optics, Phys. Reports **542**, 1-132 (2014).
- [17] G. Xu, D. Vocke, D. Faccio, J. Garnier, T. Rogers, S. Trillo, A. Picozzi, From coherent shocklets to giant collective incoherent shock waves in nonlocal turbulent flows, Nature Comm. **6**, 8131 (2015).
- [18] M. Onorato, S. Residori, F. Baronio, editors *Rogue and shock waves in nonlinear dispersive media*, (Springer, Lectures Notes in Physics, 2016).
- [19] M. Abramowitz, I. Stegun, *Handbook of mathematical functions*, Dover Publications, New-York, 1965 (sec. 13.1).
- [20] S. Skupin, M. Saffman, W. Krolikowski, Nonlocal Stabilization of Nonlinear Beams in a Self-Focusing Atomic Vapor, Phys. Rev. Lett. **98**, 263902 (2007).
- [21] A. Picozzi, S. Rica, Condensation of classical optical waves beyond the cubic nonlinear Schrödinger equation, Opt. Commun. **285**, 5440 (2012).